

## Particle Image Velocimetry Measurements of Blood Flow in a modeled Carotid Artery Bifurcation

N. A. Buchmann and M. C. Jermy

Centre for Bioengineering, Department of Mechanical Engineering  
University of Canterbury, Christchurch 8140, NEW ZEALAND

### Abstract

Cardiovascular diseases are one of the leading causes of mortality and morbidity in the western world. Amongst these diseases, atherosclerosis, a progressive narrowing of the arterial wall is one of the most severe and if untreated may lead to stroke or ischemic infarction. Fluid mechanic forces are a key player in the early development and progression of atherosclerosis and a better understanding of the interplay between haemodynamic and vascular diseases is needed. The carotid artery (CA) is one of the predominant sites of atherosclerotic plaque formation. In this work a transparent, scaled model of an average human carotid artery (AHCA) bifurcation was constructed and steady blood flow at  $Re = 290$  and  $Re = 700$  was simulated using an aqueous glycerin solution. Particle Image Velocimetry (PIV) measurements were performed in the plane of bifurcation and three axial planes in the carotid sinus. Flow inside the CA bifurcation was found to be three-dimensional with strong secondary currents due to the curvature of the vessel. An accurate method for wall shear stress (WSS) calculation along the outer internal carotid artery (ICA) wall is introduced. The method was tested against synthetically generated particle images and was found to perform best for an  $8 \times 8 \text{ pix}^2$  interrogation windows. A large low momentum flow region with low WSS along the outer ICA wall exists, posing the potential for atherosclerotic plaque formation. Calculated WSS ranged between 0 and 21. Pa and compared well with in-vivo data.

### Introduction

Atherosclerosis is a progressive narrowing of the blood carrying vessels in the human cardiovascular system. In its most severe condition atherosclerosis can lead to complete vessel occlusion and is a leading cause of stroke and ischemic infarction. Arterial stenosis is most commonly found near bends, junctions and bifurcations of large and medium arteries. It has been suggested that fluid dynamic forces, determined by the arterial geometry are a key player in the early development and progression of this disease and has been under intense investigation for the past three decades [4, 11, 12, 15, 16, 24]. The performance of the endothelial cells that line the arterial wall and, which are responsible for the health of the artery is directly influenced by steady and oscillating wall shear stress (WSS) and the primary and secondary flow pattern. WSS is a major stimulus of the endothelial structure and its biological function [21].

The carotid artery (CA) is one of the predominant sites for the formation of atherosclerotic plaque. This has been observed to frequently occur where the common carotid artery (CCA) bifurcates into the internal carotid artery (ICA) and external carotid artery (ECA). This has been understood to be a result of the presence of the carotid sinus located at the origin of the ICA. It is thought to give rise to a disturbed local haemodynamic environment with variation in WSS and complex three-dimensional flows.

Due to its severe consequences of atherosclerotic plaque formation, many studies have attempted to assess the role of local blood haemodynamic in atherogenesis. Hoecks et al. [9] and Samijo et al. [18] performed in-vivo ultrasound studies to assess WSS in human carotid arteries. Other authors performed in-vitro model studies or numerical simulations for flow visualization and quantification of blood flow in modeled arterial bifurcations. This work is reviewed in Lou and Yang [13]. Here, only the most relevant studies are summarised briefly. The early modeling work goes back to Bharadva et al. [1, 2] and Ku et al. [12] who developed a representative glass model of the averaged human carotid artery bifurcation (Y-AHCB) for flow visualisation and LDA measurements. The model was derived from a systematic angiogram study of 50 subjects and comprises the common carotid artery and the internal and external carotid artery forming a Y-shaped bifurcation. Their geometrical description of the carotid artery was used by many researchers thereafter [6, 7, 15, 16, 24]. Blood flow inside the Y-AHCB model was found to exhibit a large flow separation region on the outside wall of the ICA [13] and mean flow assuming a helical trajectory inside and downstream of the carotid sinus [1]. Wall shear stress levels were found to vary greatly over the cardiac cycle and with location, ranging from -1.3 to 0.9 Pa on the outer wall, [12] to up to 14.6 Pa, on the inner wall of the internal carotid artery [16]. Whilst the Y-shaped AHCB model remains to an extent a standard for the investigation of blood flow through the carotid bifurcation [13], it was emerging that it may not be sufficiently accurate to entirely map the physiological flow condition in the CA bifurcation [5]. Angiogram and specimen figures showed that most ICAs bend inwards after the sinus, being shaped like a tuning fork, rather than being straight as modeled in the Y-shaped geometry. Therefore, Ding et al. [5] conducted a more systematic study and found that only 8% of 74 dissected carotid bifurcations were straight. On the other hand, in more than 50% the internal and external carotid artery formed a tuning fork shaped (TF-shaped) bifurcation. The remainder were characterised as spoon-shaped bifurcation. Based on this data Ding et al. developed a TF-AHCB model to perform flow visualisation. Their flow results qualitatively agreed with those found earlier, but indicated that the helical motion inside the carotid sinus is more profound and extends further downstream than in the Y-AHCB. In addition, as the ICA bends inwards at the end of the sinus a second separation region at the inside wall was observed. This phenomena was not observed in earlier studies and is most likely due to the absence of the secondary curvature in the Y-AHCB model.

The first quantitative flow measurements in such a tuning fork shaped averaged human carotid bifurcation (TF-AHCB) thus far are reported in [3]. The present work develops a transparent scaled model of a TF-AHCB with refractive index matching and suitable for optical flow measurements. In a first step we simulate steady flow at systole and diastole and quantitatively measure blood flow and wall shear stress by digital Particle Image Velocimetry (PIV). A method for the accurate calculation of WSS from two-dimensional PIV data is

introduced. The systematic error due to overlapping interrogation windows with the wall is corrected and the method is tested on synthetically generated particle images. Results of this work will further help to understand the correlation between geometry variability and local blood flow haemodynamic as well as being a platform for further development towards patient specific flow phantoms and their investigation by PIV.

### Experimental Method

The geometry of a human averaged carotid artery bifurcation was derived from data given by Ding et al. [5]. A CAD model was constructed in STL format with some variations in curvature of the vessel walls, but were well within normal anatomical variations. The model comprises the common carotid artery (CCA) and the bifurcation into the internal (ICA) and external carotid artery (ECA) as shown in Figure 1. A physical prototype of the carotid bifurcation was created from plaster of paris using three-dimensional computer controlled printing. The thickness of each layer was approximately  $0.5\text{mm}$  and the model was scaled up to 3.2 times life size to allow more accurate flow measurements. The largest diameter at the common carotid artery was  $D = 20\text{mm}$  in the scaled model corresponding to an in-vivo diameter of approximately  $6.25\text{mm}$  and a bifurcation angle of  $50^\circ$ . All other dimensions were scaled accordingly. The planes A-C for cross-sectional flow measurements were approximately  $1.5D$  apart. From this prototype a transparent silicon rubber test section of the carotid bifurcation was constructed in a three-step casting process [3]. In brief, the exact shape of the prototype was reproduced in a female rubber cast, which was then used to create a prototype duplicate in a low melting point alloy. After solidification the duplicate was polished and embedded in a

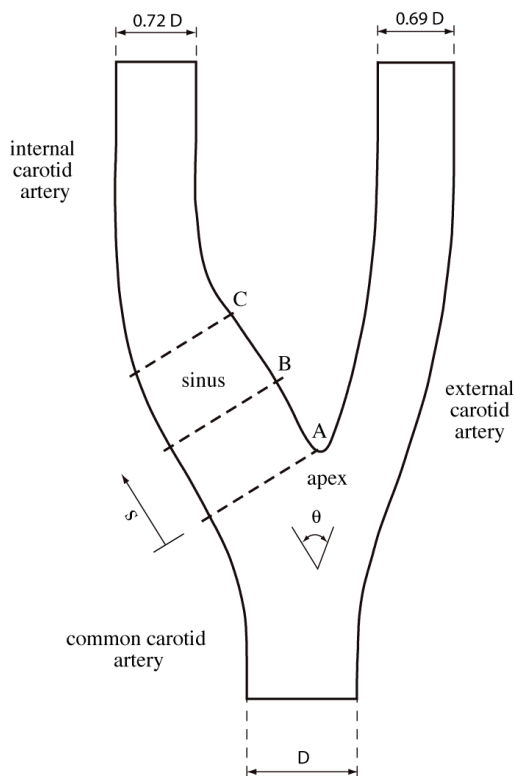


Figure 1: Schematic representation of the model geometry adapted from [5]. Dashed lines indicate the positions A-C where cross-sectional flow velocities were measured.

clear silicon resin and drained out with hot water after curing of the silicone rubber. Thus, a transparent scaled flow phantom of a human carotid artery bifurcation was constructed (Figure 2).

The model bifurcation was installed in a recirculating flow system as shown in Figure 3. Steady mean flow was supplied through a constant pressure header tank and conducted through a  $1.5\text{m}$  long pipe to the test section. A length of 75 tube diameter of straight pipe upstream of the bifurcation model ensured fully developed flow at the inlet of the common carotid artery. An electromagnetic flowmeter (Arkon MagX1) was placed upstream and a custom-made flow balance was located downstream of the internal carotid artery branch. Two valves downstream of the test section were used to adjust the individual flow rates in the internal and external carotid branch. Fluid from the downstream tank was pumped back to the header tank via a centrifugal pump. A temperature feedback control system was installed in the main tank to monitor and control the temperature of the working liquid. All pipes and tanks were insulated to reduce convective heat losses.

To avoid optical distortion of the laser beam as it travels through the three-dimensional curved flow passage and distortion of the camera image we used a refractive index matching method similar to that of Hopkins et al. [10]. The refractive index of the silicone rubber used for the phantom construction is specified as 1.43 by the manufacturer, but may vary due to differences in mixing and curing from model to model. A mixture of water and glycerin was used as a working fluid and to match the refractive index of the flow phantom. The concentration of the aqueous glycerin mixture is chosen by placing a chess board grid behind the model and noting the distortion of the gridlines. Water is gradually added to the mixture and as the target refractive index is approached, the distortion in the grid lines will disappear. Figure 2 shows the distortion of the gridlines as seen through the model when filled with water and an optimal water/glycerin mixture.

The optimum mixture was found to be 39% water and 61% glycerin by volume. The temperature dependency of the mixtures kinematic viscosity was measured with a Haak viscometer and found to vary by up to one order of magnitude over the temperature range typically found in our laboratories. The temperature dependency of the refractive index was measured with a Abbe refractometer and was negligible. Considering the increased model size and the finite measurable flow rate of the flow sensors, the Reynolds number matching requires a kinematic viscosity of the blood substitute as large as possi-

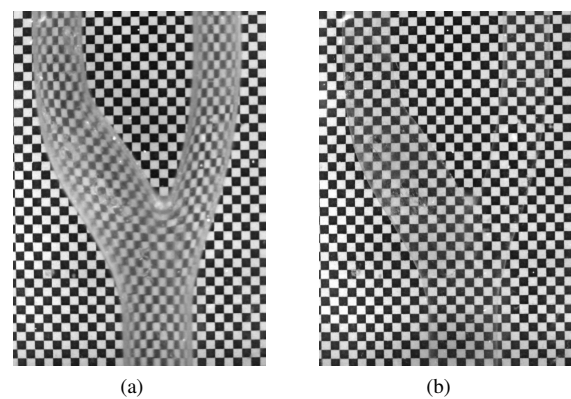


Figure 2: Distortion of the chess board grid as seen through the bifurcation model when filled with water (a) and an optimal water glycerin mixture (b).

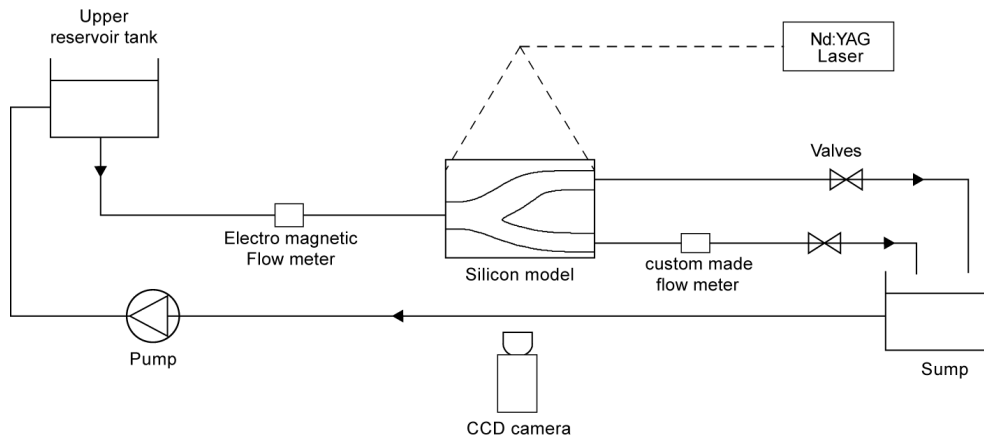


Figure 3: Sketch of the experimental setup, arrows indicate flow direction.

ble. Therefore, the working liquid was cooled by the above described setup to yield a kinematic viscosity of  $14.0 \cdot 10^{-6} m^2/s$ . The corresponding in-vivo viscosity is  $3.5 \cdot 10^{-6} m^2/s$  and a common carotid artery diameter of 6.25mm [11]. Steady flow experiments were performed at Reynolds numbers of  $Re = 290$  and  $Re = 700$  corresponding to mean and systolic flow, respectively [11]. Although the division of flow in the two daughter branches varies during the cardiac cycle [11], the flow division ratio  $\gamma = Q_{int}/Q_{ext}$  was set to 7:3 between ICA and ECA in this study.

### Velocity measurements

Digital Particle Image Velocimetry (PIV) was used to measure blood flow velocities in the plane of bifurcation and the cross-sections A-C as indicated in Figure 1. The PIV system consisted of a pulsed 120mJ Nd:Yag laser (New Wave Solo XT), a digital CCD camera (Kodak Megaplus 1.0) and optics to form a light sheet of approximately 1mm thickness. The optical setup is shown in Figure 3. The working liquid was seeded with  $10\mu m$  hollow glass spheres and sequential images of the illuminated particles were recorded on  $1008 \times 1018 \text{ pix}^2$  frames. Artificial background images were generated by averaging approximately 100 sequential particle images and subsequently subtracted from every recording. Non-flow regions were masked to impose a zero flow condition at the fluid-wall interface and to suppress wall reflections (see next section). The particle images were divided into  $64 \times 64 \text{ pix}^2$  interrogation regions and the area averaged displacement was calculated by locally cross-correlating the particle image intensities between two subsequent recordings. An overlapping factor of 50% and iterative window refinement were applied to increase and de-couple spatial resolution and dynamic range [20]. The final interrogation window size was  $8 \times 8 \text{ pix}^2$ . Window deformation based on the local velocity gradient was also applied at the final iteration step to allow for a more accurate measurement [19]. To increase the signal to noise ratio (SNR) an ensemble averaging of the correlation functions were performed as proposed by Westerweel et al. [23]. This technique is commonly used in micro-PIV and is only applicable to steady or periodic flow. An ensemble of 200 instantaneous velocity fields was used and the subsequent displacement was calculated using sub-pixel interpolation.

### Wall shear stress estimation

In order to calculate velocity gradients from velocity field data obtained by PIV, different numerical differencing schemes, including central differences, Richardson extrapolation, or least

squares methods can be applied [17]. In the vicinity of the wall interface the above methods are not applicable as they require neighboring velocity data, which are not available beyond the wall interface. In this case, forward or backward differencing needs to be performed. Common to all differencing methods is their sensitivity to grid spacing and measurement noise. Therefore, the velocity field data were smoothed with a  $3 \times 3$  unweighted convolution kernel and the grid spacing adjusted to the interrogation window size used by the PIV algorithm.

The calculation of the velocity vectors closest to the wall also introduces several bias errors due to scattering of the laser light on the fluid-wall interface and the interrogation window overlapping with the wall interface. Light scattering at the wall can be caused by slight differences in refractive indices of the fluid media and the model material (see previous section) and/or a mis-alignment of the laser light sheet. The light intensity scattered from the wall is indistinguishable from that of a particle and the cross-correlation process recognises these intensities as stationary objects. As a result, the cross-correlation peak deteriorates and velocity estimates are biased towards lower values. Another systematic error in the measurement of near wall velocities is caused by the overlapping of the interrogation windows with the wall interface. In PIV, it is assumed that the interrogation window completely surrounds a fluid volume and that the velocity vector, representing the area averaged displacement is located at the center of this window. Near the wall however, this assumption becomes invalid, as the fluid volume only occupies a fraction of the interrogation window and thus resulting in velocity magnitude and location bias. In the case of a fixed plane, this velocity bias can be eliminated by aligning the pixel rows or columns of the digital camera with the interface. However, for curved or irregular shaped interfaces the problem remains and a detailed analysis of the introduced bias is given in [8, 22].

To overcome the above limitations in the WSS calculation, we introduce a technique that is capable of eliminating the bias error and allows for reliable WSS estimates. The technique consists of the following four steps.

1. Identification of the fluid-wall interface
2. Masking of the non-flow regions and correction of the near wall vector location
3. Extraction of the tangential velocity component and its approximation by a second order polynomial
4. Calculation of the velocity gradient at the wall

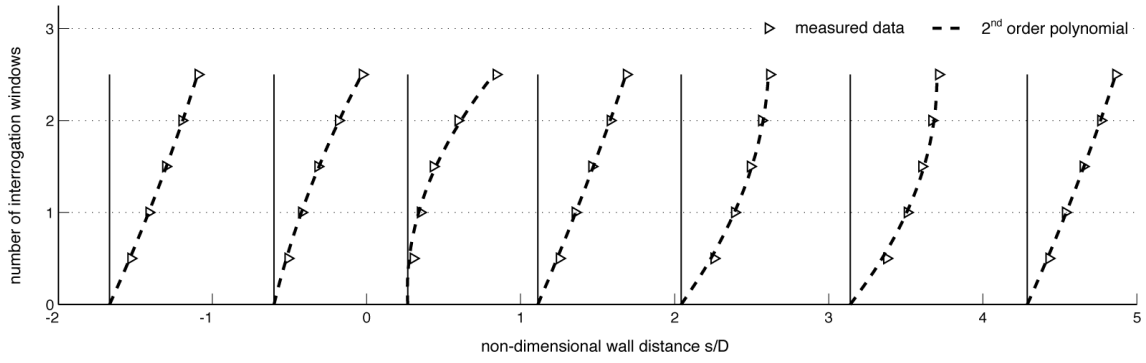


Figure 4: Tangential velocity profiles sampled at different positions along the outer ICA wall. Velocity data (triangle) are sampled over  $2 \frac{1}{2}$  interrogation windows away from the wall and a  $2^{nd}$  order polynomial is fitted (dashed line).

In the present case of rigid walls, the fluid interface can continuously be described by fitting a spline curve onto the recorded images. The extracted data points are smoothed to a length scale equal to the interrogation window size and the local orthogonal wall coordinate system  $(\xi, \eta)$  is calculated.

To eliminate the bias error originating from wall reflections, a masking of non-fluid regions with zero pixel value intensity is performed. To address the incompleteness of the interrogation regions when overlapping with the wall interface a centroid shifting technique is adapted from Hocharon et al. [8]. In the case where interrogation windows are partially occupied by fluid, the vector location is shifted to the centroid of the fluid volume within the same interrogation region. Knowing the exact position of the wall interface, the fluid centroid is determined by calculating its centre of mass.

Once the velocity vectors and their corrected locations are obtained, the near wall velocity vectors are de-composed into their tangential and normal components based on the local orthogonal wall coordinates  $(\xi, \eta)$ . It can be shown that in the vicinity of the wall, velocity profiles are of second order shape. In Figure 4, a representative collection of the tangential velocity profiles along the outer ICA wall is given. It can be clearly

seen that the measured velocity data (triangle) closely follow a  $2^{nd}$  order polynomial (dashed line) over a normal distance of approximately 2 interrogation windows. In this work, the wall normal velocity profile  $u_i(\eta)$  is thus estimated by a  $2^{nd}$  order least square fit with an imposed non-slip condition  $u_i(\eta) = 0$  at  $\eta = 0$ .

Subsequently, the local velocity gradient  $\partial u_i / \partial \eta|_w$  is calculated from the fitted tangential velocity component with a forward difference scheme. Alternatively, Hocharon et al. [8] estimated the velocity gradient with a linear scheme dividing the wall nearest velocity vector by its normal distance to the wall.

After the velocity gradient along the wall is found, the shear strain rate can be determined from the rate of the deformation tensor  $e_{ij} = (u_{ij} + u_{ji})/2$ . In the case of a two-dimensional velocity field, this expression simplifies and the local shear rate and hence WSS  $\tau_w$  can be calculated as,

$$\tau_w = \mu \left. \frac{\partial u}{\partial \eta} \right|_w \quad (1)$$

where  $\mu$  is the dynamic viscosity of the water/glycerin mixture. The measured WSS can be related to human blood flow using the Buckingham Pi Theorem and Reynolds number similarity. If the subscripts  $b$  and  $f$  refer to blood flow and the working fluid respectively, one can find the following transformation,

$$\tau_{w,b} = \frac{\rho_b}{\rho_f} \left( \frac{\mu_b D_f}{\mu_f D_b} \right)^2 \tau_{w,f} \quad (2)$$

which for the present aqueous glycerin solution amounts to  $\tau_{w,b} = 0.57 \tau_{w,f}$

The algorithm performance was tested on artificially generated particle images of a one-dimensional, fully developed pipe flow. Randomly distributed, gaussian particle images were created with a mean diameter of 2.2 pixel [17] and a seeding density of  $1/32$  particles per pixel<sup>2</sup>. The wall velocity gradient was varied between 0.1- 0.7 pixel/pixel and the images were processed with and without the centroid shifting technique. Different values for the interrogation window size were considered  $\{32 \times 32, 16 \times 16, 8 \times 8\}$  with an overlapping factor of zero and 50%. The calculated wall shear rates were averaged over the entire image. Results are shown in Figure 5 where the solid line represents the theoretical velocity gradient. Figure 5 compares the shear rate for different interrogation windows with and without overlapping and the centroid shifting technique. The results show an underestimation of the

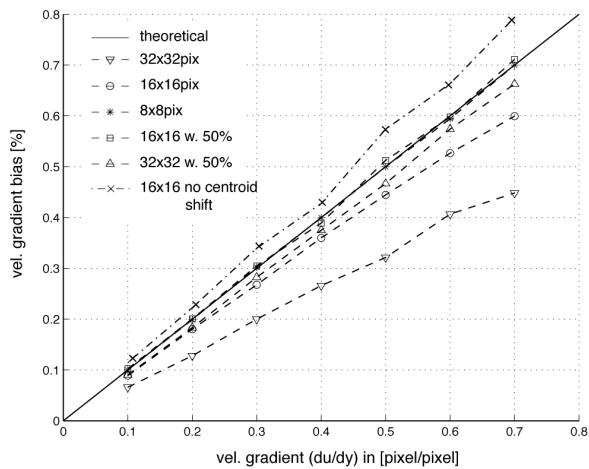


Figure 5: Simulated velocity gradient of a 1-D fully developed pipe flow; solid line represents the theoretical solution; dashed lines the simulation results for different interrogation windows, window overlapping and with and without centroid shifting.

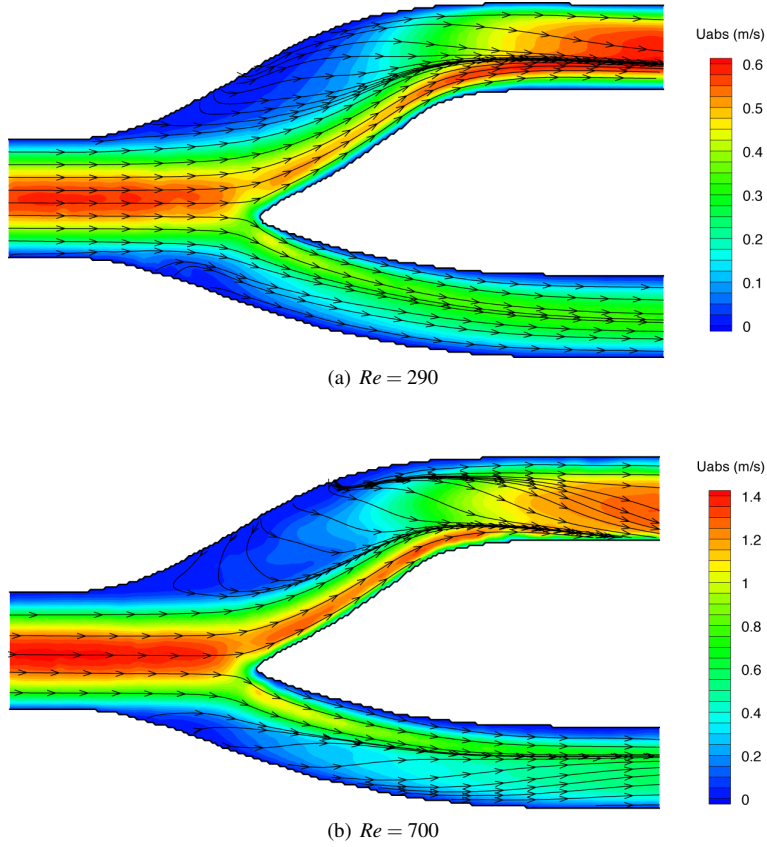


Figure 6: *In plane streamlines superimposed on velocity magnitude for (a)  $Re = 290$  and (b)  $Re = 700$ .*

shear rate for increasing shear values and larger interrogation windows. The error becomes negligible for a  $16 \times 16 \text{ pix}^2$  window with 50% overlapping, which essentially corresponds to a  $8 \times 8 \text{ pix}^2$  window. This is not surprising since smaller interrogation regions provide a greater spatial resolution and thus a more exact sampling of the spatial shear. However, for smaller windows one must guarantee an adequate number of particle image pairs per interrogation region. If the centroid shifting is not applied the current method clearly overestimates the velocity gradient. In conclusion, it can be said that the developed method provides accurate wall shear estimates for small interrogation windows (i.e.  $8 \times 8$ ,  $16 \times 16 \text{ pix}^2$ ) with an increasing uncertainty for larger velocity gradients. Thus, the method can be utilised for wall shear stress measurements in the modeled carotid artery bifurcation.

## Results and Discussion

### Axial and Secondary flow

Measurements in the plane of bifurcation were performed for  $Re = 290$  and  $Re = 700$ . Streamlines in the plane of measurements are defined as

$$\mathbf{u} \times d\mathbf{x} = 0 \quad (3)$$

where  $\mathbf{u}$  is the two-dimensional velocity data and  $d\mathbf{x}$  the in-plane streamlines. Hence, streamlines are continuous lines tangential to the in-plane velocity vector.

Figure 6 plots in-plane streamlines superimposed on the velocity magnitude. Nearest to wall, streamlines in the CCA strongly deviated to the inner wall of the carotid sinus causing a region

of reversed, low momentum flow along the outer wall of the carotid sinus. This region, classically described as a recirculation region with flow separation at the proximal sinus poses some interesting features. Rather being a closed loop in which fluid particles are entrapped, a region of reversed flow at the CCA/ICA junction is progressively restored to streamwise flow under the influence of the high momentum fluid along the inner wall. In addition, one can see the formation of one or more so called stagnation streamlines downstream of the distal sinus. Unlike reported by Ding et al.[5], flow separation along the inner wall at the distal sinus, where the ICA bends inwards was not observed in our measurements.

Axial velocity profiles in the plane of bifurcation are presented in Figure 8. The Reynolds number was 700 and the flow split between internal and external carotid artery was 7:3. Fully developed flow can be seen inside the common carotid artery prior to the bifurcation. At the bifurcation (position A), the axial velocity profiles are skewed towards the apex and remain skewed throughout the sinus. The development of the low momentum region along the outer ICA wall can clearly be seen and spans approximately 50% of the sinus volume at position B (mid sinus). As flow enters the distal carotid artery it accelerates due to the decreasing cross-sectional area. As the ICA curves inward at this point, flow along the outer wall accelerates proportionally faster producing a blunt velocity profile downstream of the carotid sinus. Flow in the external carotid artery behaves similarly, but the behavior is less marked.

The branching of the common carotid artery and the curvature of the vessel introduces a radial pressure gradient directed from the outside wall towards the apex, causing secondary flow mo-

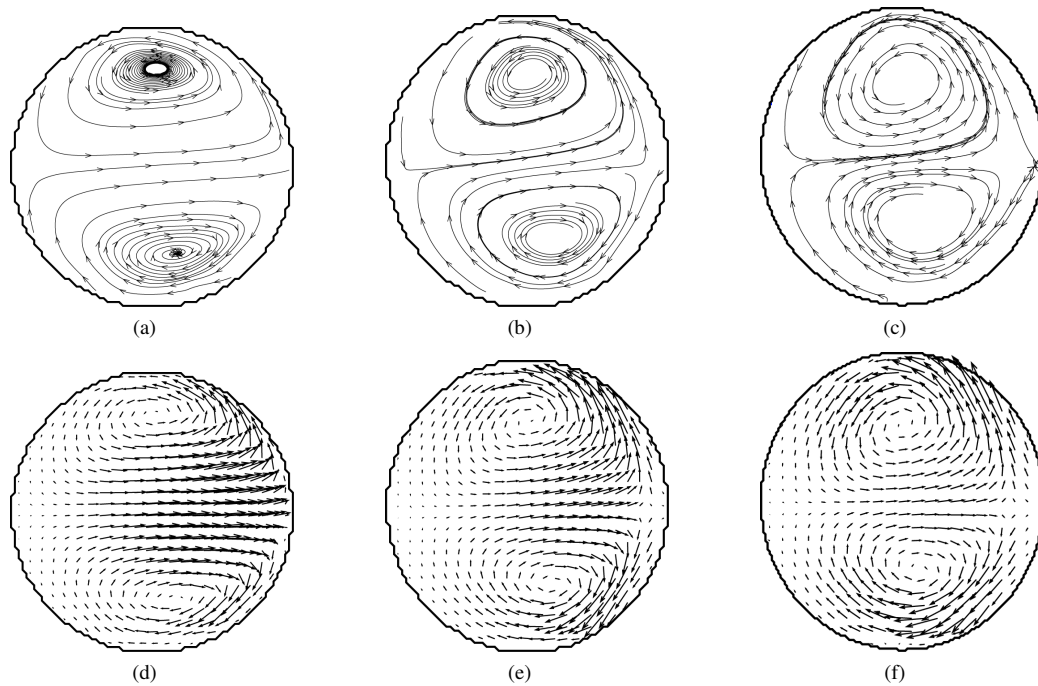


Figure 7: Secondary flow patterns at  $Re = 290$ . In-plane streamlines and velocity vectors for position A (a), (d), position B (b), (e) and position C (c), (f). In the centerline of the vessel flow is directed from the outer wall towards the flow divider (i.e from left to right).

tion. This produces a secondary vortex pair, where its size depends on the radius of curvature, vessel diameter, and flow velocity and can be expressed through the Dean number  $Dn$ . Secondary motion in the model was measured in the cross-

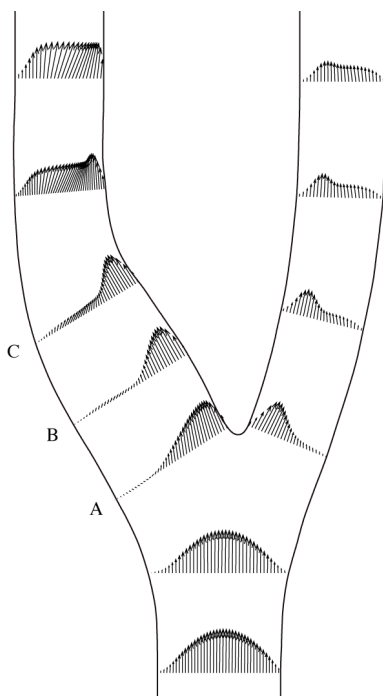


Figure 8: Axial velocity profiles for  $Re = 700$  and a flow split between ICA and ECA of 7:3.

sections of the carotid sinus as indicated in Figure 1 (plane A-C) for  $Re = 290$ . Due to the radial pressure gradient fluid moves through the centerline of the vessel towards the flow divider wall (i.e inner wall) where it separates into two streams forming two almost symmetric, counter rotating vortices, Figure 7. At plane A, Fig. 7(a,d), where the CCA bifurcates into the ICA a strong cross flow towards the apex develops with the vortex pair pushed to the upper and lower wall. This is a result of the abrupt changes in streamwise direction and the ability of the flow not to follow this change immediately. Further downstream at mid sinus (Fig. 7(b,e)) the cross flow reduces and curvature effects of the vessel become predominant exhibiting a larger vortex pair. Regions of high velocity move away from the centerline towards the upper and lower walls at the distal sinus Fig. 7(c,f).

#### Wall shear stress

Figure 9 plots the velocity gradient and wall shear stress (WSS) along the ICA outer wall. Data are computed in the plane of bifurcation and are plotted along the normalised wall distance  $s/D$ , where  $D$  is the common carotid artery diameter. The origin is defined at the begin of the carotid sinus (i.e plane A). For  $Re = 290$ , WSS is nearly constant upstream the carotid sinus with values identical to that of fully developed Poiseuille flow (i.e  $du/dn_{Poiseuille} = 0.4pix/pix$ ). At the separation point ( $s = -1$ ), the flow experiences an increase in cross-section and WSS along the outer wall rapidly decreases to values just below zero at the proximal sinus,  $s = 0$ . Flow re-attaches shortly after and WSS becomes positive again, but remains at very low values across the carotid sinus. At the distal sinus flow accelerates again with a maximum at  $s = 3$  before reaching nominal level further downstream.

In Figure 9, WSS was computed for two different interrogation windows, each with 50% overlapping. Although good agreement is achieved for moderate shear rates ( $< 0.4pix/pix$ ) the

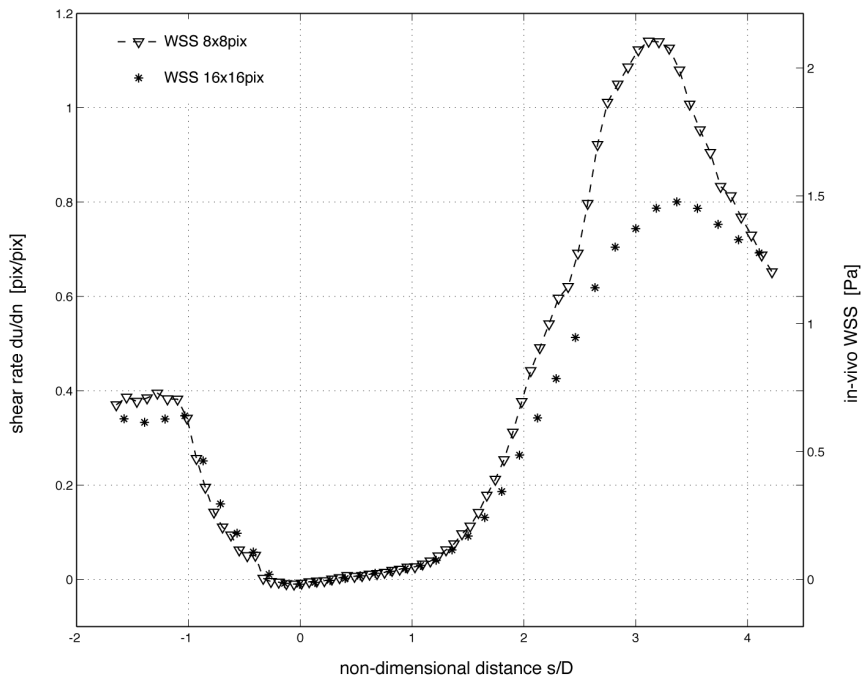


Figure 9: WSS and wall velocity gradient along the outer ICA wall obtained by two different interrogation window sizes.  $Re = 290$ .

8x8 window gives much higher shear rates in the high velocity region downstream the distal sinus. This was expected, since the smaller interrogation windows yield an increased spatial resolution and thus a more accurate sampling of the local velocity gradient.

One should keep in mind that flow in the carotid sinus is complex and three-dimensional with strong secondary flows. Hence, wall shear stress can also be expected to be highly three-dimensional. In this study, in-plane WSS was calculated from 2D PIV velocity fields and therefore only a lower bound on the WSS can be given. In order to obtain the true WSS, one needs to consider its out of plane component, which for example becomes accessible through stereoscopic PIV measurements [14].

To allow for a clinical comparison, the calculated WSS values are converted to in-vivo conditions using Equation (2). Steady mean WSS between 0 and 2.1 Pa was measured, which compares well with the findings from Samijo et al. [18] who performed in-vivo ultrasound measurements in the common carotid artery in subjects of different age and gender. Their results indicated a mean WSS of approximately 1.1 Pa and a peak value of up to 2.8 Pa. There is a strong correlation between endothelial dysfunction and areas of low mean shear stress [21]. Manifestation of intima thickening along the ICA outer wall was observed by Zarins et al. [24]. Low wall shear and flow separation inhibits or disturbs local mass transfer to and from the arterial wall. Lipoproteins may therefore be prevented from leaving the arterial wall and nutrients in the mainstream from reaching the wall [13]. Regions of low convective transport may also promote particle deposition and platelet aggregation. Another mechanism of atherogenesis is thought to occur on a bio-chemical level. In normal or high WSS regions, the endothelial cells are regularly aligned, exhibiting many atheroprotective characteristics; atherosclerosis is rare in these locations. However, in regions of low WSS the bio-chemical environment is disturbed with poorly aligned endothelial cells and reduced intracellular signaling [4]. This area still remains controversial and therefore an area of intense biological study.

## Conclusion

In this work, we presented a methodology to simulate steady blood flow in a scaled model of a tuning fork shaped averaged human carotid bifurcation (TF-AHCB), a geometrical variation of the carotid bifurcation that has so far been little studied. The refractive index and the Reynolds number were matched in a scaled physical model and Particle Image Velocimetry (PIV) measurements were performed in the plane of bifurcation and at three spanwise locations in the carotid sinus. For the Reynolds numbers under investigation, the flow exhibited a complex three-dimensional motion with strong secondary currents in the carotid sinus. A region of reversed, low momentum fluid along the outer ICA wall was observed, giving rise to low wall shear stresses (WSS). A method for calculating in-plane spatial WSS from PIV velocity data was presented using a second order polynomial approximation of the velocity profile in the vicinity of the wall. The bias error inherent to the near wall estimation in PIV was corrected with a masking and centroid shifting technique. Results from measurement and simulation showed an increase in accuracy of the estimated WSS when reducing the size of the interrogation windows. WSS measurements along the outer ICA wall for  $Re = 290$  revealed a flow separation point approximately one diameter upstream the proximal sinus and a low WSS region along the entire sinus. Good agreement in measured WSS was found with physiological data. Future work will focus on enhancing the robustness of the WSS estimation, the simulation of pulsatile flow, and the development of patient specific models.

## Acknowledgment

The research was funded by the Neurological Foundation of New Zealand and NB would like to acknowledge the Royal Society of New Zealand for their financial support.

## References

- [1] Bharadvaj, B. K., Mabon, R. F. and Giddens, D. P., Steady flow in a model of the human carotid bifurcation. 1 – flow visualization, *Journal of Biomechanics*, **15**, 1982, 349 – 362.
- [2] Bharadvaj, B. K., Mabon, R. F. and Giddens, D. P., Steady flow in a model of the human carotid bifurcation. 2 - laser-doppler anemometry measurements, *Journal of Biomechanics*, **15**, 1982, 363 – 378.
- [3] Buchmann, N. A., Jermy, M. C. and David, T., Experimental investigation of blood flow in the brain by means of particle image velocimetry - a preliminary study, in *Proceedings of the Fifth International Conference on Fluid Mechanics, Shanghai, China, 2007*.
- [4] Comerford, A., *Computational Models of Endothelial and Nucleotide Function*, Ph.D. thesis, University of Canterbury, New Zealand, 2007.
- [5] Ding, Z., Wang, K., Li, J. and Cong, X., Flow field and oscillatory shear stress in a tuning-fork-shaped model of the average human carotid bifurcation, *Journal of Biomechanics*, **34**, 2001, 1555 – 1562.
- [6] Gijsen, F. J. H., Palmén, D. E. M., van der Beek, M. H. E., van de Vosse, F. N., van Dongen, M. E. H. and Janssen, J. D., Analysis of the axial flow field in stenosed carotid artery bifurcation models - Iida experiments, *Journal of Biomechanics*, **29**, 1996, 1483–1489.
- [7] Gijsen, F. J. H., van de Vosse, F. N. and Janssen, J. D., Influence of non-Newtonian properties of blood on the flow in large arteries: Steady flow in a carotid bifurcation model, *Journal of Biomechanics*, **32**, 1998, 601 – 608.
- [8] Hochareon, P., Manning, K. B., Fontaine, A. A., Tarbell, J. M. and Deutsch, S., Wall shear-rate estimation within the 50cc penn state artificial heart using particle image velocimetry, *Journal of Biomechanical Engineering*, **126**, 2004, 430 – 437.
- [9] Hoeks, A. P. G., Samijo, P. J. and Reneman, R. S., Assessment of wall shear rate in humans: an ultrasound study, *Journal of Vascular Investigation*, **1**, 1995, 108–117.
- [10] Hopkins, L. M., Kelly, J. T., Wexler, A. S. and Prasad, A. K., Particle image velocimetry measurements in complex geometries, *Experiments in Fluids*, **29**, 2000, 91–95.
- [11] Ku, D. N. and Giddens, D. P., Laser doppler anemometer measurements of pulsatile flow in a model carotid bifurcation, *Journal of Biomechanics*, **20**, 1987, 407–421.
- [12] Ku, D. N., Giddens, D. P., Zarins, C. K. and Glagov, S., Pulsatile flow and atherosclerosis in the human carotid bifurcation. positive correlation between plaque location and low oscillating shear stress, *Arteriosclerosis, Thrombosis, and Vascular Biology*, **5**, 1985, 293 – 302.
- [13] Lou, Z. and Yang, W.-J., Biofluid dynamics at arterial bifurcations, *Critical Reviews in Biomedical Engineering*, **19**, 1992, 455–493.
- [14] Nguyen, C. V. and Wells, J. C., Direct measurement of fluid velocity gradients at a wall by piv image processing with stereo reconstruction, *Jornal of Visualization*, **9**, 2006, 199–208.
- [15] Perktold, K. and Resch, M., Numerical flow studies in human carotid artery bifurcations. basic discussion of the geometric factor in atherogenesis, *Journal of Biomedical Engineering*, **12**, 1990, 111 – 123.
- [16] Perktold, K., Resch, M. and Peter, R. O., Three-dimensional numerical analysis of pulsatile flow and wall shear stress in the carotid artery bifurcation, *Journal of Biomechanics*, **24**, 1991, 409 – 420.
- [17] Raffel, M., Willert, C. E. and Kompenhans, J., *Particle Image Velocimetry - A Practial Guide*, Springer-Verlag Berlin-Heidelberg, 1998.
- [18] Samijo, S. K., Willigers, J. M., Barkhuysen, R., Kitslaar, P. J. E. H. M., Reneman, R. S., Brands, P. J. and Hoeks, A. P. G., Wall shear stress in the human common carotid artery as function of age and gender, *Cardiovascular Research*, **39**, 1998, 515–522.
- [19] Scarano, F., Iterative image deformation methods in piv, *Meas. Sci. Technol.*, **13**, 2002, R1–R19.
- [20] Scarano, F. and Riethmuller, M. L., Iterative multigrid approach in piv image processing with discrete window offset, *Experiments in Fluids*, **26**, 1999, 513–523.
- [21] Traub, O. and Berk, B. C., Laminar shear stress : Mechanisms by which endothelial cells transduce an atheroprotective force, *Arteriosclerosis, Thrombosis, and Vascular Biology*, **18**, 1998, 677–685.
- [22] Tsuei, L. and Savas, O., Treatment of interfaces in particle image velocimetry, *Experiments in Fluids*, **29**, 2000, 203 – 214.
- [23] Westerweel, J., Geelhoed, P. F. and Lindken, R., Single-pixel resolution ensemble correlation for micro-piv applications, *Experiments in Fluids*, **37**, 2004, 375–384.
- [24] Zarins, C., Giddens, D., Bharadvaj, B., Sottiurai, V., Mabon, R. and Glagov, S., Carotid bifurcation atherosclerosis. quantitative correlation of plaque localization with flow velocity profiles and wall shear stress, *Circulation Research*, **53**, 1983, 502–514.